

## Classification of quark and gluon jets in hot QCD medium with deep learning

---

Yi-Lun Du,<sup>a,b,\*</sup> Daniel Pablos<sup>c</sup> and Konrad Tywoniuk<sup>a</sup>

<sup>a</sup>*Department of Physics and Technology, University of Bergen,  
Postboks 7803, 5020 Bergen, Norway*

<sup>b</sup>*Department of Physics, University of Oslo,  
Sem Sælands vei 24, 0371 Oslo, Norway*

<sup>c</sup>*INFN, Sezione di Torino, via Pietro Giuria 1,  
I-10125 Torino, Italy*

*E-mail: [yilun.du@uib.no](mailto:yilun.du@uib.no)*

Deep learning techniques have shown the capability to identify the degree of energy loss of high-energy jets traversing hot QCD medium on a jet-by-jet basis. The average amount of quenching of quark and gluon jets in hot QCD medium actually have different characteristics, such as their dependence on the in-medium traversed length and the early-developed jet substructures in the evolution. These observations motivate us to consider these two types of jets separately and classify them from jet images with deep learning techniques. We find that the classification performance gradually decreases with increasing degree of jet modification. In addition, we discuss the predictive power of different jet observables, such as the jet shape, jet fragmentation function, jet substructures as well as their combinations, in order to address the interpretability of the classification task.

\*\*\* *Particles and Nuclei International Conference - PANIC2021* \*\*\*

\*\*\* *5 - 10 September, 2021* \*\*\*

\*\*\* *Online* \*\*\*

---

\*Speaker

## 1. Introduction

The deconfined QCD matter created in heavy ion collisions has been seen to behave as a strongly-coupled viscous fluid [1–3], commonly known as the quark-gluon plasma (QGP). Jets, collimated sprays of hadrons generated in a hard QCD process, are witnesses to the evolution of the QGP. Partons from the jet interact with the hot medium, losing energy and experiencing a variety of modifications, known as jet quenching phenomena. Therefore, observed high-energy hadrons and jets can be used as probes with which to extract the transport properties of the QGP [4, 5]. A clear indication of jet quenching can be seen by calculating the ratio of the yields of high-energy hadrons or jets measured in heavy ion collisions over those measured in proton-proton (pp) collisions [6–8], which presents a strong suppression. Additionally, one can also study the medium modification of jets by analyzing their substructures, again usually done by comparing the results of both samples at the same transverse energy [9–13]. However, one needs to take into account the presence of a selection bias [14–17] in such comparisons. Due to the steeply falling jet spectrum, very quenched jets will be under-represented after imposing the selection criteria. In other words, the selected, surviving jet samples generally possess narrower early-time substructures that tend to lead to less jet energy loss, hindering our interpretation about what true medium-induced modifications of jet substructures are. These ambiguities can be mitigated by estimating the energy loss of each individual jet.

In this and our previous work [18, 19], we use deep learning techniques to estimate, on a jet-by-jet basis, the amount of energy loss, quantified through the variable  $\chi \equiv p_T/p_T^{\text{initial}}$  suffered by jets in the QGP.  $p_T$  is the transverse momentum of a given jet in the presence of a medium with cone size  $R$ , and  $p_T^{\text{initial}}$  is the transverse momentum of the *same* jet had there been no medium, see [18] for further details on how to establish such a correspondence. The jet samples in PbPb collisions are simulated in the hybrid strong/weak coupling model [20–22], while those in pp collisions rely on PYTHIA8 event generator [23, 24]. In this regression task, we train a convolutional neural network (CNN), taking the jet images as inputs, in order to predict  $\chi$  in a supervised manner. As shown in Fig. 8 of Ref. [18], our framework delivers very good performance. Usually one selects jets according to their final, measured energy, such as above a certain threshold,  $p_T > p_T^{\text{cut}}$ . With the estimated jet energy loss at hand, one can have an initial energy selection instead, i.e., considering  $p_T^{\text{initial}} > p_T^{\text{cut,initial}}$ <sup>1</sup>. We show that this novel selection method can effectively remove the selection bias, informing us of the true medium modifications of jet substructures [18], and helping us get access to the genuine spatial and angular distribution of the jets created in the nuclear overlap region in the collisions [19].

Quark- and gluon-initiated jets experience different evolutions, both in vacuum and in the medium. For this reason, it would be interesting to explore the differences between quark and gluon jets, and classify them – see previous and related work [25, 26]. In the following, we first present their different quenching behavior. We then use deep learning techniques to classify them and analyze the predictive power of the different jet observables for this task. Finally, we summarize and conclude.

<sup>1</sup>At the same time we also require  $p_T > p_T^{\text{cut}}$  to ensure that it is within the scope where the neural network is trained. As long as  $p_T^{\text{cut,initial}}$  is sufficiently higher than  $p_T^{\text{cut}}$ , it means that we have considered all the jets of  $p_T^{\text{initial}} > p_T^{\text{cut,initial}}$ .

## 2. Different quenching behavior

In our work [18], we generate approximately 250,000 jets at  $\sqrt{s} = 5.02$  ATeV for PbPb collisions at 0-5% centrality within the hybrid strong/weak coupling model, with the single parameter  $\kappa_{sc}$  tuned to reproduce hadron and jet suppression at the LHC [27]. Reconstructed jets with FastJet 3.3.1 [28] using anti- $k_T$  [29] algorithm and  $R = 0.4$  are required to be within  $|\eta| < 2$  and to have momentum  $p_T^{\text{jet}} > 100$  GeV. In Fig. 1, we show the prediction performance of energy loss ratio  $\chi$  for quark and gluon jets, respectively. One can see that the performance is similar and the network has good compatibility. In the large- $\chi$  regime, the performance on quark jets is slightly better, while in the small- $\chi$  regime, the performance on gluon jets is slightly better.

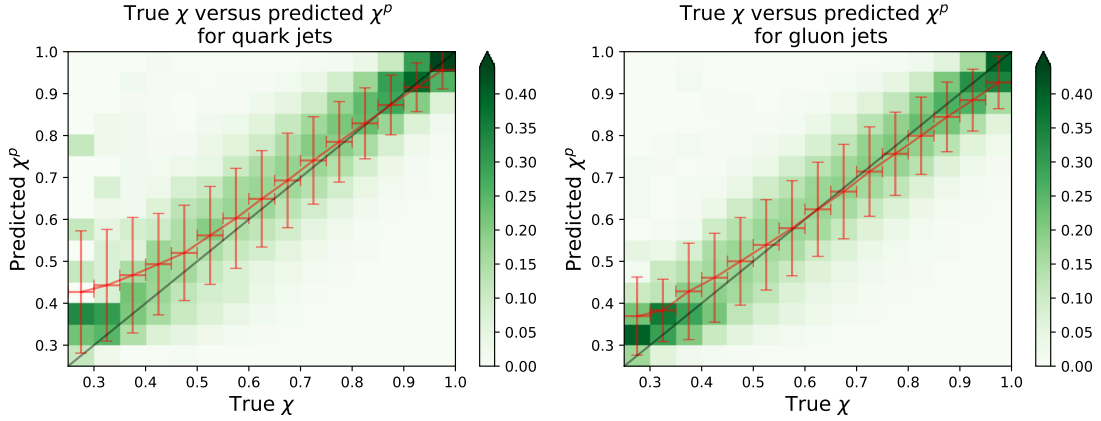


**Figure 1:** CNN prediction performance on quark (left) and gluon (right) jets. The green color represents the probability of predicted  $\chi$  along y-axis given true  $\chi$  in 2-D histogram, where each column is self-normalized. The red line with error bar quantifies the average and standard deviation of the predicted  $\chi$  within the given true  $\chi$  bin.

The evolution of quark and gluon jets in vacuum is simulated using PYTHIA 8.244 [23, 24]. Their microscopic processes and splitting functions are different. Both the splitting angle as well as the available phase space that can trigger medium-induced radiation are larger, on average, for gluon jets. However, and differently to pQCD computations, the dependence of quark and gluon energy loss in holographic approaches is different only by the ratio of the Casimirs with a reduced

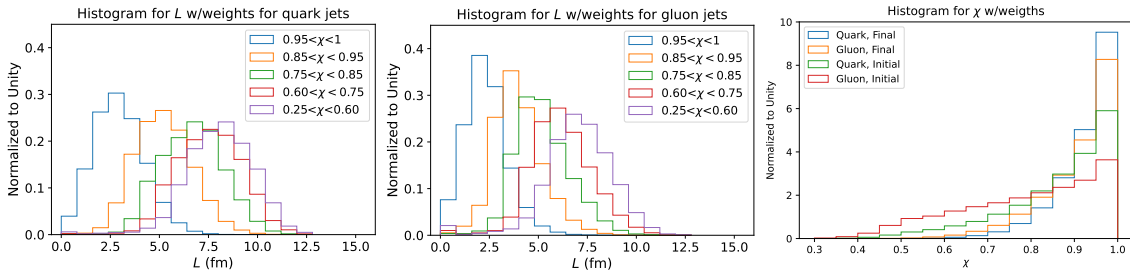


**Figure 2:** Left (middle) panel: Distributions of the in-medium traversed length of quark (gluon) jets within different ranges of true values of  $\chi$ . Right panel: The true  $\chi$  distributions of quark and gluon jets with *Final* energy selection, and *Initial* energy selection.

power,  $(9/4)^{1/3}$  [30]. Therefore, gluons will lose more energy when traversing the same length. In the left and middle panels of Fig. 2, we show the in-medium traversed distance  $L$  distribution in the QGP for both quark and gluon jets, sliced in different  $\chi$  bins, where  $L$  is defined by the traverse momentum  $p_{Ti}$  weighted sum of traversed length  $L_i$  (in the fluid rest frame) of all the jets constituents, see Ref. [18] for details. One can see that jet energy loss increases with the in-medium traversed length. The average energy loss of gluon jets is, as expected, more sensitive to the traversed length. We observe that if we can classify the quark and gluon jets successfully, it will help us pin down the correlation between  $L$  and the amount of energy loss, thereby pushing forward our jet tomographic study [19]. Another reason for distinguishing quark/gluon jets is to check the universality of energy loss for different processes, e.g. comparing dijet events (with a mix of quark- and gluon-initiated jets) with boson-jets (where the parton recoiling from the boson is predominantly a quark).

In the right panel of Fig. 2, we show the true  $\chi$  distributions of quark and gluon jets with the final ( $p_T > 200$  GeV) and initial energy selections ( $p_T^{\text{initial}} > 200$  GeV,  $p_T > 100$  GeV). One can see how with the initial energy selection, gluon jets do lose more energy on average and consequently a larger proportion of very quenched jets are included in the sample. With the final energy selection, and even though the existence of the selection bias, there are still more quenched samples in the gluon jets ensemble.

### 3. Pre-analysis and Classification Results

In Fig. 3, we show the average of  $p_T$ -normalized quark and gluon jet images in 5 different  $\chi$  bins and the Pearson correlation coefficient between  $\chi$  and each pixel of the unnormalized jet images (the value belongs to  $[-1,1]$ , and the positive one means positive correlation and vice versa, please check Ref. [18] for more details). Here, all the jet images of  $33 \times 33$  size are rotated and flipped according to certain procedure – we again defer the interested reader to Ref. [18]. One can see that with the increase of energy loss, quark and gluon jets show the same qualitative characteristics, i.e., there are more soft particles at large angles within the jet cone. But the quantitative details are different. Losing the same amount of energy, gluon jets look wider than quark jets, and there are more soft particles around the periphery of the jet. In fact, gluon jets losing a certain amount of energy, i.e. at a given  $\chi_g$ , look like quark jets that lost significantly more energy, i.e. with a  $\chi_q \ll \chi_g$ . Notwithstanding, generally speaking, gluon jets are wider and more densely populated than quark jets. From the Pearson correlation coefficient image, one can see that the correlation between the gluon jet substructures and its energy loss is more pronounced. These observations bring both opportunities and challenges to the task of classifying quark and gluon jets in the medium.

In Fig. 4, we show the classification performance of quark and gluon jets with CNN, including the results of the vacuum jets as well as the medium jets, both inclusive and differential in  $\chi$ , which are characterized by the receiver operating characteristic curves (ROC curves). The  $x$ -axis is the quark jet receiving efficiency, while the  $y$ -axis is the gluon jet rejection efficiency. The identification of quark and gluon jets by the network varies with the classification threshold given by the output of the network. The closer the area under the ROC curves (AUC) is to 1, the more successful the classification task is. Here, the architecture of the CNN is very similar to the one used in Ref. [18], except for a change in the final output layer of the network to two neurons, adding a Sigmoid

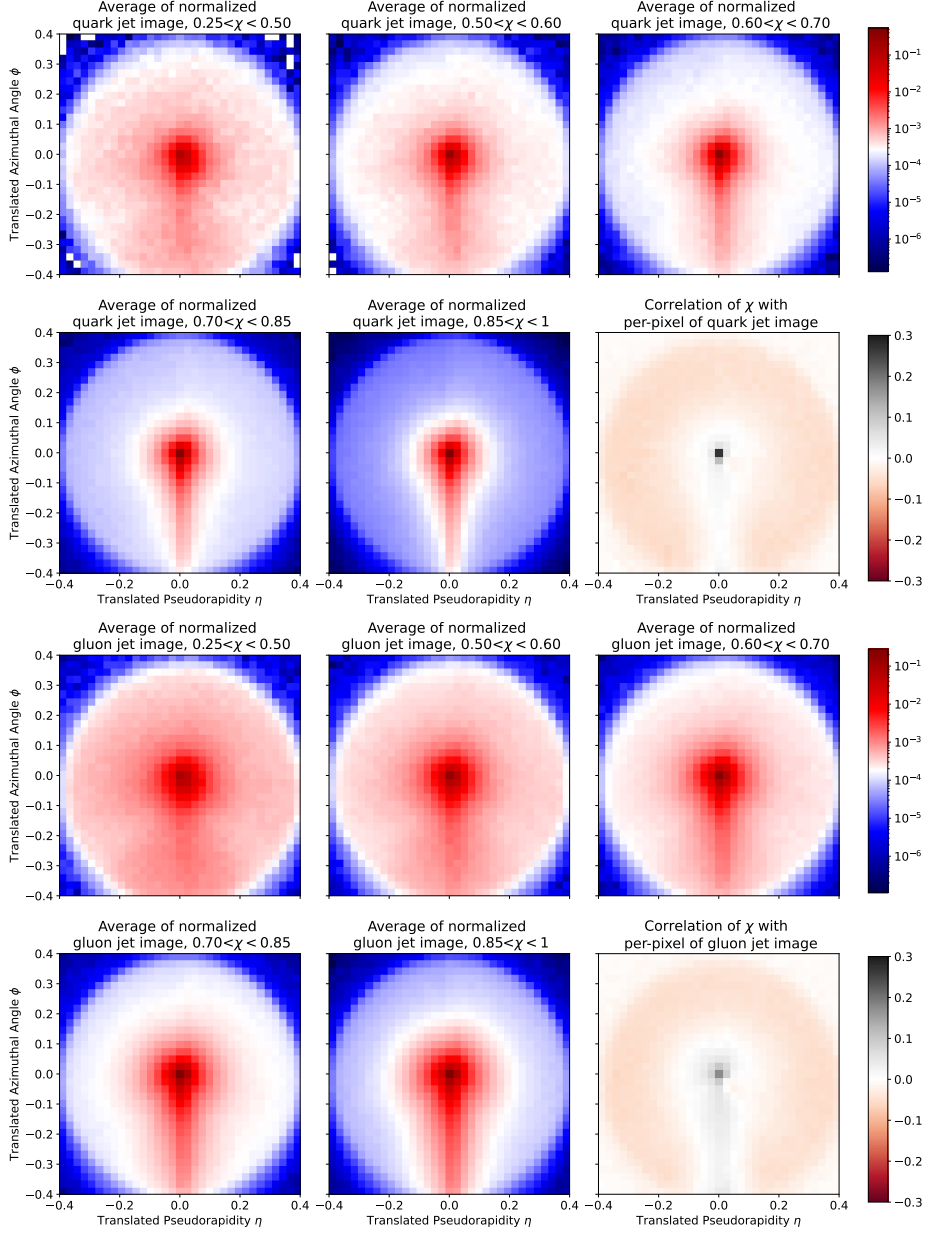


**Figure 3:** The average of quark/gluon jet image normalized by jet  $p_T$  within 5 different  $\chi$  cut bins (3 in the top row and 2 in the bottom row, respectively) and Pearson correlation coefficient of  $\chi$  with per-pixel of the unnormalized jet image (rightmost panel in the bottom row).

activation function for a binary classification task and changing the loss function of the network to the cross-entropy one. Overall, the classification accuracy of quark and gluon jets in the medium is a bit lower than that in the vacuum, which agrees with Ref. [25], and its relative decrease depends on the fraction of the quenched jets. This is consistent with the observation made from the results of the classification for medium jets with different  $\chi$ , i.e., the greater the energy loss is, the more difficult the classification becomes.

In addition to employing jet images as input, we also use some jet observables and their

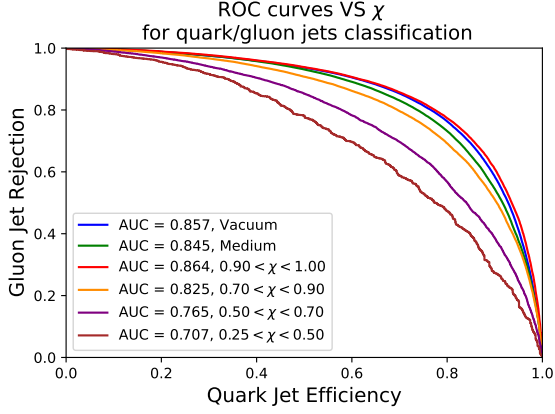


**Figure 4:** ROC curves of quark efficiency versus gluon rejection for jets in pp collisions and jets in PbPb collisions, both for inclusive and sliced in  $\chi$  samples.

Input (size)	Accuracy
Jet shape (8)	72.2%
JFF (10)	73.0%
Jet features (7)	73.6%
JFF, jet shape (18)	74.9%
JFF, jet shape, features (25)	75.8%
Jet image (33×33)	75.9%

**Table 1:** Classification performance with different inputs. Jet features include: jet  $p_T$ ,  $z_g$ ,  $n_{SD}$ ,  $R_g$ ,  $M$ ,  $M_g$ , Multiplicity.

combinations as the inputs to a fully-connected neural network to perform the same classification task for comparison. The architecture of the network is also similar to the one used in Ref. [18]. These jet observables include jet shape, jet fragmentation function (JFF) and some single-valued jet observables, such as jet  $p_T$ , jet mass  $M$ , jet multiplicity and some groomed jet substructures, like the momentum sharing between the subjets  $z_g$ , Soft-Drop multiplicity  $n_{SD}$ , the angle of the first hard splitting  $R_g$ , jet groomed mass  $M_g$  given by the Cambridge/Aachen (C/A) algorithm [31, 32] and the Soft-Drop (SD) algorithm [33], please check Ref. [18] for details. The classification performance from these jet observables inputs is listed in Tab. 1. One can find that the performance given by the jet shape, jet fragmentation function and jet features increase. This ordering is different from that in the regression task of the energy loss prediction [18], which shows the different sensitivities of these jet observables to different tasks. Similar to the regression task, combining all these observables as input can reproduce the performance given by the jet images, which can serve as an indirect interpretability for the success of the quark/gluon jets classification using the jet images as input.

#### 4. Summary and Outlook

In this work, we first showed the good compatibility of the CNN by presenting its prediction performance on the energy loss of quark and gluon jets, respectively, yielding quite similar results. We presented the different features of quark and gluon jets after quenching and used deep learning techniques to classify them. It has been found that the greater the energy loss is, the more difficult it is to classify the jets. For now, our study has been purely phenomenological or based on results from selected Monte Carlo models. Given this interesting results, it would also be appealing to pursue a more general theoretical understanding of quark and gluon jet modifications in order to take full advantage of this tagging in the future.

## Acknowledgments

This work is supported by the Trond Mohn Foundation under Grant No. BFS2018REK01 and the University of Bergen. Y. D. thanks the support from the Norwegian e-infrastructure UNINETT Sigma2 for the data storage and HPC resources with Project Nos. NS9753K and NN9753K. D. P. has received funding from the European Union's Horizon 2020 research and innovation program under the Marie Skłodowska-Curie grant agreement No. 754496.

## References

- [1] K. Ackermann, N. Adams, C. Adler, Z. Ahammed, S. Ahmad, C. Allgower, J. Amsbaugh, M. Anderson, E. Anderssen, H. Arnesen, *et al.*, *Phys. Rev. Lett* **86**, 402 (2001).
- [2] K. Aamodt, B. Abelev, A. A. Quintana, D. Adamova, A. Adare, M. Aggarwal, G. A. Rinella, A. Agocs, S. A. Salazar, Z. Ahammed, *et al.*, *Phys. Rev. Lett* **105**, 252302 (2010).
- [3] K. Aamodt, B. Abelev, A. A. Quintana, D. Adamova, A. Adare, M. Aggarwal, G. A. Rinella, A. Agocs, A. Agostinelli, S. A. Salazar, *et al.*, *Phys. Rev. Lett* **107**, 032301 (2011).
- [4] Y. Mehtar-Tani, J. G. Milhano, and K. Tywoniuk, *Int. J. Mod. Phys. A* **28**, 1340013 (2013), [arXiv:1302.2579 \[hep-ph\]](#) .
- [5] G.-Y. Qin and X.-N. Wang, *Int. J. Mod. Phys. E* **24**, 1530014 (2015), [arXiv:1511.00790 \[hep-ph\]](#) .
- [6] K. Adcox, S. Adler, N. Ajitanand, Y. Akiba, J. Alexander, L. Aphecetche, Y. Arai, S. Aronson, R. Averbek, T. Awes, *et al.*, *Phys. Rev. Lett.* **88**, 022301 (2001).
- [7] C. Adler, Z. Ahammed, C. Allgower, J. Amonett, B. Anderson, M. Anderson, G. Averichev, J. Balewski, O. Barannikova, L. Barnby, *et al.*, *Phys. Rev. Lett.* **89**, 202301 (2002).
- [8] B. Abelev *et al.* (ALICE), *JHEP* **03**, 013 (2014), [arXiv:1311.0633 \[nucl-ex\]](#) .
- [9] S. Chatrchyan *et al.* (CMS), *Phys. Lett. B* **730**, 243 (2014), [arXiv:1310.0878 \[nucl-ex\]](#) .
- [10] S. Chatrchyan *et al.* (CMS), *Phys. Rev. C* **90**, 024908 (2014), [arXiv:1406.0932 \[nucl-ex\]](#) .
- [11] S. Acharya *et al.* (ALICE), *Phys. Lett. B* **776**, 249 (2018), [arXiv:1702.00804 \[nucl-ex\]](#) .
- [12] A. M. Sirunyan *et al.* (CMS), *Phys. Rev. Lett.* **120**, 142302 (2018), [arXiv:1708.09429 \[nucl-ex\]](#) .
- [13] A. M. Sirunyan *et al.* (CMS), *JHEP* **10**, 161 (2018), [arXiv:1805.05145 \[hep-ex\]](#) .
- [14] H. Zhang, J. F. Owens, E. Wang, and X.-N. Wang, *Phys. Rev. Lett.* **98**, 212301 (2007), [arXiv:nucl-th/0701045](#) .
- [15] H. Zhang, J. F. Owens, E. Wang, and X.-N. Wang, *Phys. Rev. Lett.* **103**, 032302 (2009), [arXiv:0902.4000 \[nucl-th\]](#) .

- [16] J. Casalderrey-Solana, G. Milhano, D. Pablos, and K. Rajagopal, *JHEP* **01**, 044 (2020), [arXiv:1907.11248 \[hep-ph\]](#) .
- [17] J. Brewer, Q. Brodsky, and K. Rajagopal (2020) [arXiv:2009.03316 \[hep-ph\]](#) .
- [18] Y.-L. Du, D. Pablos, and K. Tywoniuk, *JHEP* **21**, 206 (2020), [arXiv:2012.07797 \[hep-ph\]](#) .
- [19] Y.-L. Du, D. Pablos, and K. Tywoniuk, arXiv preprint [arXiv:2106.11271](#) (2021).
- [20] J. Casalderrey-Solana, D. C. Gulhan, J. G. Milhano, D. Pablos, and K. Rajagopal, *JHEP* **2015**, 175 (2015).
- [21] J. Casalderrey-Solana, D. C. Gulhan, J. G. Milhano, D. Pablos, and K. Rajagopal, *JHEP* **03**, 053 (2016), [arXiv:1508.00815 \[hep-ph\]](#) .
- [22] J. Casalderrey-Solana, D. Gulhan, G. Milhano, D. Pablos, and K. Rajagopal, *JHEP* **03**, 135 (2017), [arXiv:1609.05842 \[hep-ph\]](#) .
- [23] T. Sjostrand, S. Mrenna, and P. Z. Skands, *Comput. Phys. Commun.* **178**, 852 (2008), [arXiv:0710.3820 \[hep-ph\]](#) .
- [24] T. Sjöstrand, S. Ask, J. R. Christiansen, R. Corke, N. Desai, P. Ilten, S. Mrenna, S. Prestel, C. O. Rasmussen, and P. Z. Skands, *Comput. Phys. Commun.* **191**, 159 (2015).
- [25] Y.-T. Chien and R. Kunnawalkam Elayavalli, (2018), [arXiv:1803.03589 \[hep-ph\]](#) .
- [26] J. Brewer, J. Thaler, and A. P. Turner, *Phys. Rev. C* **103**, L021901 (2021).
- [27] J. Casalderrey-Solana, Z. Hulcher, G. Milhano, D. Pablos, and K. Rajagopal, *Phys. Rev. C* **99**, 051901(R) (2019), [arXiv:1808.07386 \[hep-ph\]](#) .
- [28] M. Cacciari, G. P. Salam, and G. Soyez, *Eur. Phys. J. C* **72**, 1896 (2012), [arXiv:1111.6097 \[hep-ph\]](#) .
- [29] M. Cacciari, G. P. Salam, and G. Soyez, *JHEP* **04**, 063 (2008), [arXiv:0802.1189 \[hep-ph\]](#) .
- [30] S. S. Gubser, D. R. Gulotta, S. S. Pufu, and F. D. Rocha, *JHEP* **10**, 052 (2008), [arXiv:0803.1470 \[hep-th\]](#) .
- [31] Y. L. Dokshitzer, G. Leder, S. Moretti, and B. Webber, *JHEP* **08**, 001 (1997), [arXiv:hep-ph/9707323](#) .
- [32] M. Wobisch and T. Wengler, in *Workshop on Monte Carlo Generators for HERA Physics (Plenary Starting Meeting)* (1998) pp. 270–279, [arXiv:hep-ph/9907280](#) .
- [33] A. J. Larkoski, S. Marzani, G. Soyez, and J. Thaler, *JHEP* **05**, 146 (2014), [arXiv:1402.2657 \[hep-ph\]](#) .